Study of all-pass optical micro-ring resonators using titanium- and zinc oxides on an insulating platform via atomic layer deposition

J. D. Castro-Toscano[a,b], R. Salas-Montiel[c], D. Jauregui-Vazquez[a], H. Tiznado[b],
E. G. Lizarraga-Medina[d], A. G. Navarrete-Alcala[a], and H. Marquez-Becerra[a,*]

[a] *Departamento de Óptica, Centro de Investigación Científica y de Educación Superior de Ensenada, Apartado Postal 2732, Ensenada, BC 22860, México.*
[b] *Centro de Nanociencias y Nanotecnología, Universidad Nacional Autónoma de México, Apartado Postal 14, 22800, Ensenada, B.C, México.*
[c] *Laboratory Light, Nanomaterials, and Nanotechnology - L2n CNRS UMR 7076. Université de Technologie de Troyes, 10004, Troyes, France.*
[d] *Universidad Autónoma de Baja California, 22260, Blvd Universitario 1000 Valle de las Palmas, Tijuana, B.C.*
[*] *e-mail: hmarquez@cicese.mx*

Received 23 April 2024; accepted 16 December 2024

Atomic layer deposition (ALD) is a versatile technique to grow thin films for a wide range of applications including energy conversion and electronics. Materials deposited on insulating platforms through ALD can expand their use in optics and photonics. In this work, we present the design of an integrated optics all-pass micro-ring resonators based on measured optical properties of ALD materials, particularly, titanium- and zinc oxides (TiO_2 and ZnO on insulator). For optical communication applications, zinc oxide on an insulator (ZOI) provides mode confinement of 46%, an evanescent decay of 855 nm, and a quality factor of up to 10^4 at 1550 nm. Atomic layer deposited core materials on an insulator provide an effective alternative for optics and photonics.

Keywords: High refractive index materials; atomic layer deposition; channel waveguide; all-pass optical ring resonator; numerical analysis; finite element method.

DOI: https://doi.org/10.31349/RevMexFis.71.041303

1. Introduction

Devices based on optical waveguides for data transmission are a potential solution to satisfy the telecommunication demand for higher bandwidth and faster data communication, aiming to overcome the bottlenecks in data transfer [1, 2]. As a consequence, several devices in the area of integrated optics have been developed: directional couplers [3], power divisors [4], and ring resonators [5]. Optical ring resonators based on a circular loop and channel waveguides play a critical role in various applications, including optical processing filters [6], switching/routing micro-devices [7], optical delay lines [8], biosensors [9], and micro-laser cavities [10]. These devices warrant analysis with a focus on compatibility with Si/SiO_2 wafers, facilitating their integration into optoelectronics devices.

The performance of the ring resonator and the bus based on optical channel waveguides is very sensitive to effective refractive index, optical confinement, and evanescent field that depend on dimensions of waveguide cross-section and core/cladding optical properties. Hence, it is necessary to consider width and thickness tolerances induced by fabrication techniques in the designing process, i.e., atomic layer deposition (ALD) and electron-beam lithography; in which the waveguide thickness can be controlled by regulating the number of nanolayers deposited during ALD process, and the width of the channel waveguide by electro-lithography process, respectively [11]. ALD technique is a fabrication method that produces high-quality nanolayers of thickness controlled by dosing vapors of reactants on the substrate and repeating reaction cycles until the desired film thickness is obtained [12, 13]. Atomic layer deposition (ALD) has been demonstrated to be a quite promising technology for the fabrication of low-loss optical waveguides [14].

Most contributions to optical ring resonators have been based on silicon (Si) and silicon nitride (SiN) waveguides [15–17]. There are a few contributions related to optical ring resonators based on: titanium oxide (TiO_2) [18, 19] and zinc oxide (ZnO) [20, 21]. As a strategy towards nanophotonics devices, several core materials i.e. Al_2O_3, ZnO, and TiO_2, are being developed using the ALD technique on SiO_2/Si wafers in our facilities [12, 22, 23]. In this work, the design of an optical ring resonator based on ZnO and TiO2 sub-wavelength channel waveguides on SiO_2/Si substrate is presented. The design challenges of an all-pass optical ring resonator (AOR) involve reducing bending losses, a narrow linewidth (full-width half maximum, FWHM), a high-quality factor (Q-Factor), and the extinction ratio, parameters that will determine if the AOR is suitable to be used in optoelectronic micro devices.

This study aims to demonstrate that the optical ring resonators fabricated using the ALD technique exhibit competitive optical properties, making them well-suited for telecommunication applications due to the precise control of thin-thin layer deposition. Additionally, we validate that devices based on ZnO and TiO_2 materials perform effectively in telecommunications systems. Their high refractive indices enable the miniaturization of waveguide structures, facilitating sub-wavelength design creation. This capability allows these devices to support single-mode propagation and resonator activities at a wavelength of 1550 nm, achieving quality factor values exceeding 5000.

2. Methodology

2.1. Theoretical background

In general, a ring resonator consists of a looped optical waveguide and a coupling mechanism to access the loop. The AOR scheme based on a circular and straight channel waveguides is shown in Fig. 1. The circular and straight channel waveguides are named ring and bus, respectively. Cross-section parameters for each waveguide are the width (w) and thickness (h) focus to only propagate single modes, and the looped optical waveguide has an internal radius (R_{int}), and external radius (R_{ext}), and (R) as the ring radius at the half of the waveguide. The interface materials involved in the AOR are the core (ZnO and TiO_2), cladding (air), and substrate (SiO_2/Si). The signal traveling in the bus with a certain bandwidth is coupled towards the ring, separated by a distance gap d_g, where certain wavelengths will be filtered.

A simple loop is created by taking an output of a generic directional coupler and feeding it back to the input, as shown in Fig. 1. The AOR exhibits a periodic cavity resonance; when the wavelength travels through the ring, it acquires a phase shift corresponding to a multiple of 2πrad. The principle of operation of AOR is based on two components: a coupling force and a feedback path. The fundamental relation between the incident beam $(E_{\mathrm{i}1})$, the transmitted beam $(E_{\mathrm{t}1})$, and the circulating fields ($E_{\mathrm{i}2}$ and $E_{\mathrm{t}2}$) belonging to a resonator are derived by combining the coupler relationships

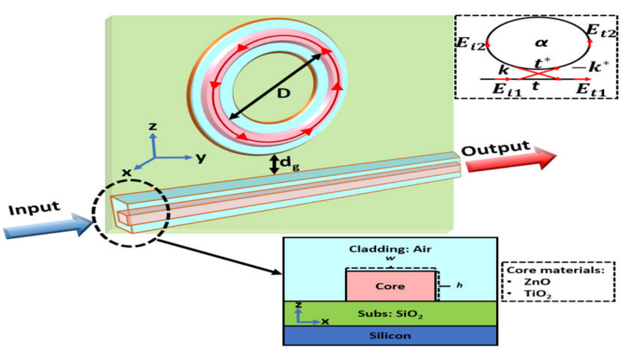

FIGURE 1. The cross-section of the channel waveguide and the scheme of the proposed AOR. The thickness and the width of the cross-section channel waveguide are the variables h and w; d_g is the coupling distance gap and D is the ring diameter.

with the optimal feedback path, being the complex amplitudes E are normalized. The optical ring resonator presents the following matrix related to the incident, transmitted, and propagated electric fields:

$$\begin{pmatrix} E_{t1} \\ E_{t2} \end{pmatrix} = \begin{pmatrix} t & k \\ -k^* & t^* \end{pmatrix} \begin{pmatrix} E_{i1} \\ E_{i2} \end{pmatrix}, \tag{1}$$

The self-coupling (k) and cross-coupling (t) coefficients satisfy the relationship $|\mathrm{k}|^2 + |\mathrm{t}|^2 = 1$. The asterisk $(*)$ denotes the complex conjugate of the coupler's parameters. To simplify the model, we assume the transmitted beam is equal to 1 ($\mathrm{E}_{i1} = 1$). Thus, a round trip in the ring is defined by:

$$E_{i2} = \alpha \cdot e^{i\theta} E_{t2}, \tag{2}$$

Here, α represents the ring's loss coefficient, with $\alpha = 0$ indicating a fully lossy ring. The phase shift θ corresponds to the single-pass phase over the ring's circumference, expressed as $\theta = \omega L/c$. The circumference length is given by $L = 2\pi R$, where ω is the angular frequency $\omega = k\mathrm{c}_0 = 2\pi\mathrm{c}_0/\lambda$, c_0 is the speed of light in a vacuum, and c is the phase velocity of the ring mode $\mathrm{c} = \mathrm{c}_0/n_{\text{eff}}$. By incorporating the effective refractive index (n_{eff}), the vacuum wavenumber can be seamlessly included in the propagation constant for the ring's coupling constant.

$$\beta = k \cdot n_{\text{eff}} = \frac{2\pi n_{\text{eff}}}{\lambda}, \tag{3}$$

Combining Eqs. (1) and (2), we obtain:

$$E_{t1} = \frac{-\alpha + t \cdot e^{-j\theta}}{-\alpha t^* + e^{-j\theta}}, \tag{4}$$

$$E_{i2} = \frac{-\alpha k^*}{-\alpha t^* + e^{-j\theta}}, \tag{5}$$

$$E_{t2} = \frac{-k^*}{1 - \alpha t^* e^{j\theta}}. \tag{6}$$

We are focused on the transmission power $P_{\mathrm{t}1}$ related to the bus output.

$$P_{t1} = |E_{t1}|^2 = \frac{\alpha^2 + |t|^2 - 2\alpha|t|\cos(\theta + \phi_t)}{1 + \alpha^2|t|^2 - 2\alpha|t|\cos(\theta + \phi_t)}, \tag{7}$$

Here, $t = |t|\exp(j\phi_t)$, where $|t|$ represents the coupling losses and ϕ_t is the phase of the coupler. At resonance, when $(\theta + \phi_t) = 2\pi n$, where n is an integer, the following expression is derived:

$$P_{t1} = |E_{t1}|^2 = \frac{(\alpha - |t|)^2}{(1 - \alpha|t|)^2}. \tag{8}$$

Detailed information can be found in Ref. [24].

2.2. Atomic layer deposition

ALD is a conformal manufacturing process that produces uniform and homogeneous films. The principle operation is obtained by sequentially dosing reagent vapors onto the substrate, growing a monolayer after achieving a cycle at a temperature that allows the precursors to react [25]. Then, to obtain a specific film thickness, it is necessary to repeat those cycles, obtaining a homogeneous and conformal thin film with highly precise control. ALD is a widely studied technique that reduces fabrication costs by avoiding material waste. It is worth mentioning that the type of precursors depends on the specific material being grown. For ZnO and TiO_2, the precursors are diethylzinc (DEZ) and tetrakis(dimethylamino)titanium (TDMAT), respectively. It is important to recall that the TDMAT precursor must be heated at 60°C to increase the vapor pressure.

In this contribution, thin films of ZnO and TiO_2 were grown on different Si/SiO_2 substrates using the Beneq TFS200 equipment, reaching different reactor temperatures: 200°C for ZnO and 250°C for TiO_2. Here, each material's nitrogen (N_2) flow quality was used: $<< 10^{-13}$ ppm O_2. The deposition cycle was different for each high refractive index material sample, consisting of introducing the precursor for ZnO (DEZ dose: 40 ms) and TiO_2 (TDMAT dose: 50 ms), then purging with N_2 for ZnO (750 ms) and TiO_2 (3 s). An oxidizing pulse of H_2O for ZnO (75 ms) and TiO_2 (3 s) was introduced, followed by a final purge with N_2 at the same values mentioned. The number of cycles necessary to grow 500 nm (ZnO) and 390 nm (TiO_2) were 2604 and 8125, respectively. The growth rates (GPC) for ZnO and TiO_2 were 1.92 Å/cycle and 0.48 Å/cycle, respectively.

3. Results and discussion

After the synthesis of core waveguide materials, optical properties such as refractive index, and effective refractive index of propagation modes of waveguides need to be determined. These parameters are required to obtain the intensity distribution of the propagation modes, optical waveguide layout and transmission wavelength spectrum of optical resonators; which results are described next.

3.1. Dispersion curve measurements

After ALD synthesis, optical material dispersions were obtained from ellipsometer measurements as shown in Fig. 2. By using the technique variable angle spectroscopy ellipsometry (VASE) with the equipment J.A. Woollam Model M-2000, the refractive index values (n) of synthesized layers (ZnO and $\mathrm{TiO_2}$) were measured in the wavelength range from 500 nm to 1000 nm. Thus, the samples were analyzed on silicon wafer substrates (Si) with a thermal oxide layer of 3 μm ($\mathrm{SiO_2}$) and thin layers of 500 nm (ZnO) or 390 nm ($\mathrm{TiO_2}$), this thickness has been proved by fiber-waveguide coupling to calculate propagation losses, showing an appropriate single-mode propagation [12, 26]. To fulfill the material dispersion in the wavelength range of 1000 to 1600 nm required for further processes, the cubic B-spline extrapolation method was used. This was necessary to calculate the waveguide core material's refractive index before computing the modal analysis of the cross-section channel waveguide.

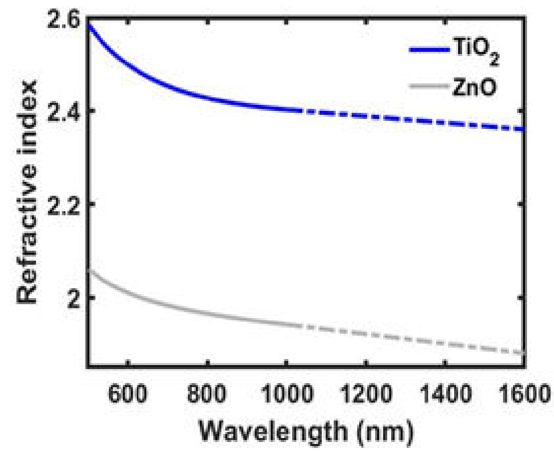

FIGURE 2. Measured material dispersion curve from the ALD synthesized core materials ZnO, and TiO_2 from the 500 to 1600 nm wavelength range. The continuous line represents the ellipsometer values of the ALD synthesized materials, while the dashed lines represent the estimation of the dispersion curve.

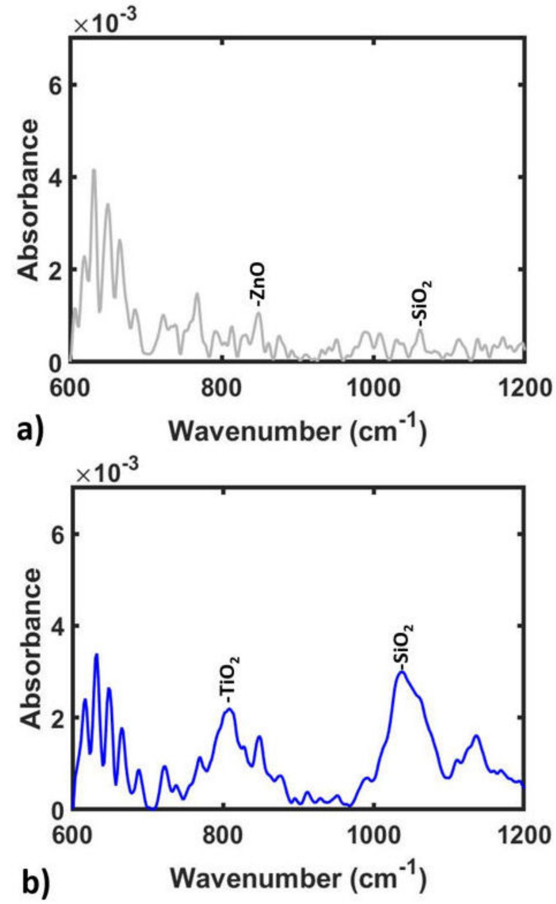

FIGURE 3. IR spectra of a) crystalline ZnO 500 nm film thickness and b) amorphous TiO_2 390nm film.

The refractive index values at 1550 nm wavelength are 2.36372 ($\mathrm{TiO_2}$) and 1.88581 (ZnO). These values are used to calculate the effective refractive index values (n_{eff}) for the waveguide structures. By using the equipment Bruker Tensor 27-IR, the FTIR spectrum for each of the samples was obtained as shown in Fig. 3. The vibration peaks belonging to SiO_2 are related to the stretching modes at 1100 to 1000 cm^{-1} [27]. For the TiO_2 and ZnO structures, the vibration peaks are in the wavenumber range 700-1000 cm^{-1} [28, 29].

3.2. Channel waveguide propagation mode properties

The cross-section waveguide described in Fig. 1 was analyzed to calculate the $n_{\rm eff}$ and modal confinement for the propagation mode. Considering the interfaces refractive index of cladding (air: 1.00), substrate (SiO_2: 1.44), and the core values shown in Fig. 2. With the thickness layer (h) mentioned in the previous section for each of our samples, the optimal width (w) for fundamental mode were analyzed for ZnO and TiO_2, as shown in Fig. 4 for an operating wavelength of 1550 nm.

For Fig. 4, the effective dispersion curve resolution analysis for the width was from 0.100 μm ranging from 0.5 μm to 3.0 μm. The dashed circle represents the existence of hybrid modes for each of our effective dispersion curves, where ZnO has a more extensive area to not stimulate hybrid modes (TM$_0$-TE$_1$) because it is a material with a lower refractive index value compared with TiO_2 [30]. The yellow region represents the effective condition to ensure the existence of the TE$_0$ fundamental mode. The dashed red line represents the refractive index of the SiO_2 substrate; then, if the $n_{\rm eff}$ of the structure is higher than this value, modal propagation exists. It is essential to point out that a 200 nm error margin for the electro-lithography technique must be considered for the maximum width to propagate the fundamental mode (TE$_0$) for 1600 nm (ZnO) and 900 nm (TiO_2). As a consequence, the following widths will be analyzed: 1400 nm (ZnO) and 700 nm (TiO_2). The $n_{\rm eff}$ values for each structure are the following: 1.5946 (ZnO) and 1.7732 (TiO_2). It should also be mentioned that the more significant value of the refractive index represents a higher confinement. Figure 5 shows the intensity distribution of the eigenmode (TE$_0$) for each selected material, and Table I shows waveguide parameters.

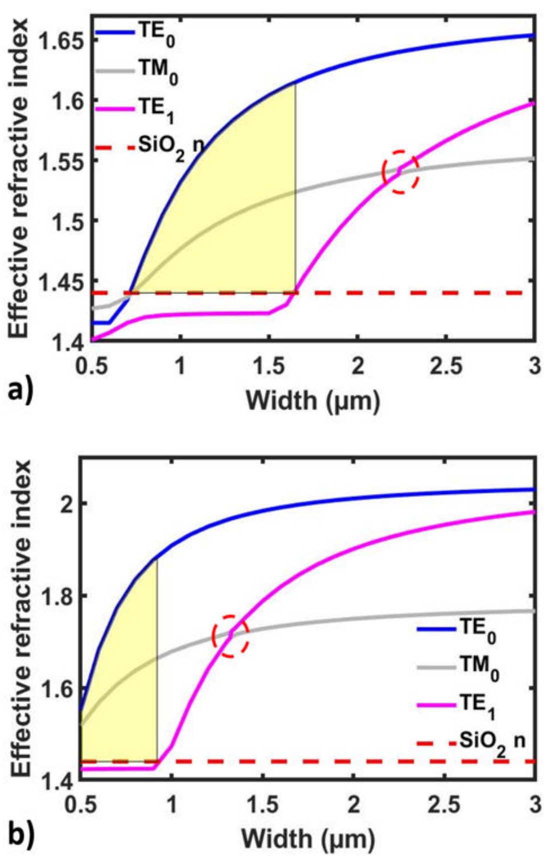

FIGURE 4. Calculated dispersion curve of the modes TE$_0$, TM$_0$, and TE$_1$ at 1550 nm wavelength operation from a) ZnO, and b) TiO$_2$. The yellow area represents an optical channel waveguide with a range of width values for single mode operation for a film thickness of a) 500 nm, and b) 390 nm. The dashed circle represents the existence of hybrid modes (TM$_0$-TE$_1$).

TABLE I. Cross-section waveguide parameters.

Material	Height (nm)	Width (nm)	$n_{\rm eff}(TE_0)$
ZnO	500	1400	1.5946
TiO$_2$	390	700	1.7732

TABLE II. Intensity distribution percentage for cross-section channel waveguide materials.

Material	Core	Substrate	Cladding
ZnO	46%	33%	21%
TiO$_2$	40%	27%	33%

Considering the structure configuration for fundamental modal propagation, it is necessary to calculate the intensity distribution percentage for the whole cross-section waveguide interface, as shown in Table II. As shown, the channel waveguide material with a high effective refractive index value shows lower modal intensity confinement (TiO_2). Meanwhile, the channel waveguide material with a lower effective refractive index value presents higher modal confinement for single-mode operation. However, the channel waveguide dimensions should be considered; here, the TiO_2 dimensions are smaller.

The evanescent wave intensity distribution for the channel waveguide materials configuration was computed. This property provides information about the capacity of coupling light to another optical channel waveguide. For the evanescent wave study, the intensity profile of Fig. 5 was analyzed for the different cross-section optical channel waveguides configuration. The white dashed line represents the section where the intensity profile was analyzed.

The modal profile distribution indicates the excitation of down-peaks at the core-cladding interface, which can be considered weakly guided modes [31–33]. The evanescent wave distance reach for each channel waveguide material configuration at 0.01% of the distribution was: 855 nm (ZnO) and 716 nm (TiO_2); as can be seen in Fig. 5, these

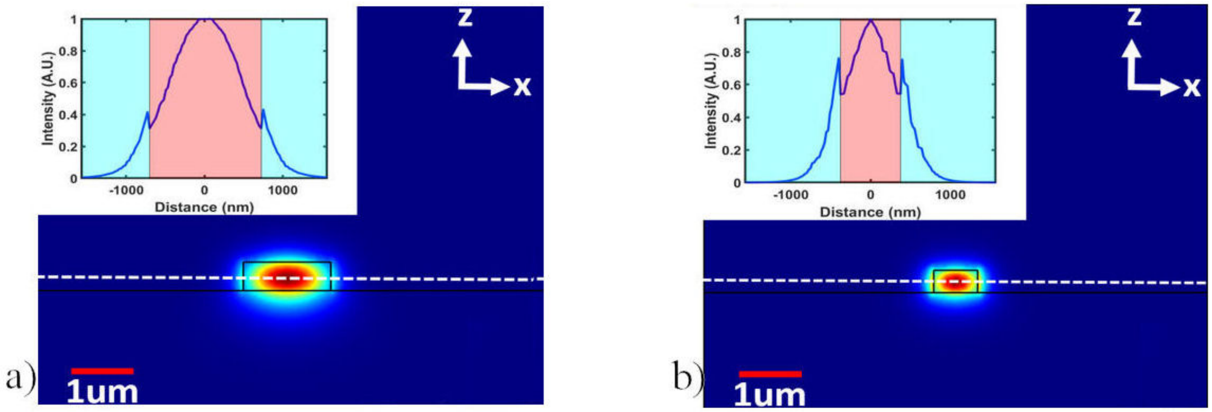

FIGURE 5. The TE_0 intensity distributions and their cross-section intensity profile at 1550 nm wavelength operation for a) ZnO ($h = 500$ nm, $w = 1400$ nm, and $n = 1.88581$), and b) TiO_2 ($h = 390$ nm, $w = 700$ nm, and $n = 2.36372$).

distances are suitable for fabrication techniques such as electro-lithography.

3.3. Properties of the AOR design

Once the modal and evanescent intensity distribution of the fundamental propagation mode for the structures were calculated, the next step is to design the ring resonator. It is necessary to consider the filtering mode characteristics for the AOR design. Here, the cross-section for the curved waveguide would be the same as the straight bus waveguide, with a 60 μm ring radius (r), and the design must be centered to obtain at least nine resonant modes; moreover, these modes must be suitable for the C band of telecommunications. These would be our initial design parameters, which represent a maximum of 4.22 nm for the free spectral range (FSR), which is the space between each resonant mode. It is important to note that mode propagation has not offset for the ring radius curvature, meaning that the intensity distribution is centered in the curved waveguide.

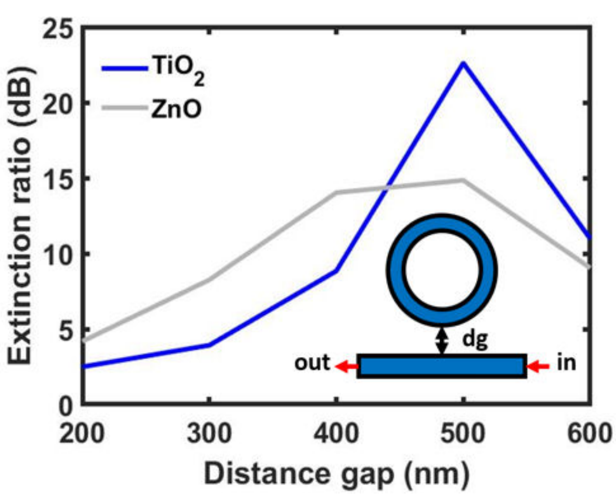

FIGURE 6. Extinction ratio for each material considering the distance gap ranges of 200 to 600 nm from the telecommunication wavelength range C band.

To estimate the optical properties of an optical ring radius (r) of 60 μm was chosen, and then the d_g was analyzed. The total length for the straight channel waveguide satisfies $l = 2{*}r{+}w$. The resolution analysis for d_g was 100 nm ranging from 200 nm to 600 nm, and wavelength range C Band (1528 nm to 1566 nm). The extinction ratio was calculated, as shown in Fig. 6. The higher extinction values are 14.84 dB (ZnO) and 22.60 dB (TiO_2) for their corresponding d_g of 500 nm for both materials.

Figure 7 presents the filter analysis of the better configuration of the extinction ratio belonging to ZnO, showing how the AOR works when the resonant wavelength is traveling in it.

TABLE III. AOR's filtering parameters for 60 μm radius.

Parameters	TiO_2	ZnO
Transmittance peak	0.9465	0.9893
Transmittance deep	0.0047	0.0184
Extinction ratio (dB)	22.6021	14.8425
Average FSR (nm)	3.56	3.95
FWHM (nm)	0.4396	0.22188
F	8.0969	17.8020
Q-Factor	3533	7005

TABLE IV. Ring resonator performance in terms of radius variation for each ALD synthesized material.

ZnO	60 μm	120 μm	180 μm
FWHM (nm)	0.2218	0.1596	0.1210
Q-Factor	7005	9742	12842
Bending losses (dB/cm)	-19.4699	-4.4377	-7.3069
TiO_2	60 μm	120 μm	180 μm
FWHM (nm)	0.4396	0.3550	0.3082
Q-Factor	3533	4381	5045
Bending losses (dB/cm)	-0.9708	-0.3103	-0.4845

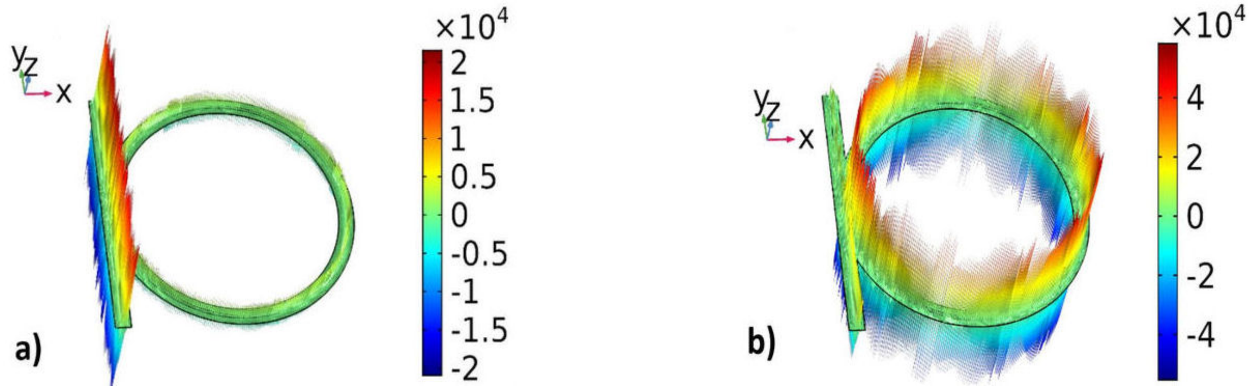

FIGURE 7. Filtering analysis for the ZnO configuration $d_g = 500$ nm: a) the wavelength at 1552.56 nm passing through the Bus, b) the wavelength at 1554.40 nm filtered towards the ring.

TABLE V. Comparison of the fabrication methods, materials and structural dimensions of different optical wavelength devices.

Device	Clad/Core/Subs	Synthesis method	λ [μm]	Subwavelength	Losses (dB/cm)	Year	Cite
SWG	SiO_2/Si/SiO_2	N/M	1.55	Yes	18	2006	[35]
SWG	Air/Si/SiO_2	PECVD	1.52-1.56	Yes	18	2020	[36]
SWG	SiO_2/Si/SiO_2	N/M	1.55	Yes	2.6	2018	[37]
AOR	Air/GaAs/AlGaAs	N/N	5.9972	No	18	2019	[38]
AOR	AlGaAs/GaAs/AlGaAs	N/M	1.55	Yes	40	2000	[39]
AOR	Air/SiGe/Si	N/M	4.8	No	0.2	2023	[40]
AOR	Air/Ge/Si	N/M	4.6	Yes	1.7	2022	[41]
COW	Air/TiO_2/SiO_2	RFMS	0.6328	No	9.7	2011	[42]
COW	Air/TiO_2/SiO_2	DCS	0.633-1.55	Yes	7.5	2015	[43]
MRR	Air/TiO_2/SiO_2	IBS	1.55	No	3.1	2020	[44]
COW	Air/ZnO/SiO_2	N/M	0.6328	No	6	2022	[45]
POW	Air/ZnO/SiO_2	RCMS	0.677	No	38-14	2009	[46]
AOR	Air/ZnO/SiO_2	ALD	1.55	Yes	19.46 - 4.43	2024	*P
AOR	Air/TiO_2/SiO_2	ALD	1.55	Yes	0.97 - 0.31	2024	*P

Note: *SWG: Subwavelength gratings; *COW: Channel optical waveguides; *MRR: micro ring resonator; POW: Planar optical waveguide; N/M: Not mentioned; PECVD: Plasma enhanced chemical vapor deposition; RFMS: Radio frequency magnetic sputtering; DCS: Direct Current Sputtering; IBS: Ion beam sputtering; RCMS: Reactive cathode magnetron sputtering. *P: In this paper.

The filtering analysis was made considering the optical signal filtered near the 1555 nm range, as shown in Fig. 8. Configuration based on TiO_2 and ZnO demonstrates suitable optical linewidth.

As shown, for the resonant wavelength operation at: 1553.68 nm (TiO_2) and 1554.4 nm (ZnO). Then, considering this as a resonant wavelength (λ_{res}), it is possible to calculate their optical parameters: free spectral range $\mathrm{FSR} = \lambda^2/n_{\mathrm{eff}}L'$, full-width half maximum $\mathrm{FWHM} = (1 - r\alpha)\lambda_{\mathrm{res}}^2/\pi n_{\mathrm{eff}} L\sqrt{r\alpha}$, quality factor $\mathrm{Q-Factor} = \lambda_{\mathrm{res}}/\mathrm{FWHM}'$, and finesse $\mathrm{F} = \mathrm{FSR}/\mathrm{FWHM}'$, where cavity length (L), coupling coefficient (r), and attenuation coefficient (α). All the optical parameters mentioned above for each structure are shown in Table III. The ZnO optical parameters show modest Q and the FWHM is attractive for telecommunication filtering applications (small FWHM and maximal filtering transmission). It is important to note that $\mathrm{TiO_2}$ exhibits comparable and relatively low performance, respectively. However, the $\mathrm{Q-factor}$ should be improved.

As can be observed, the $\mathrm{Q-Factor}$ is a parameter that needs improvement; thus, we chose the optical ring radius as a parameter to study the $\mathrm{Q-Factor}$. The following radius is analyzed: 120 μm and 180 μm (shown in Fig. 9), to provide a reliable device [8, 9, 34]. As shown in Table IV, structures with larger radius increase the quality factor variable. As the ring radius increases, the linewidth becomes narrower. ZnO and TiO_2 exhibit a bending losses increment for the maximum radius. Notably, single-mode operation affects the bending losses in this configuration, with a ring radius limit where bending losses reach a minimum. Beyond this limit, the losses increase due to the extended propagation length. Despite this effect, the losses are minimal and do not affect the performance of the AOR.

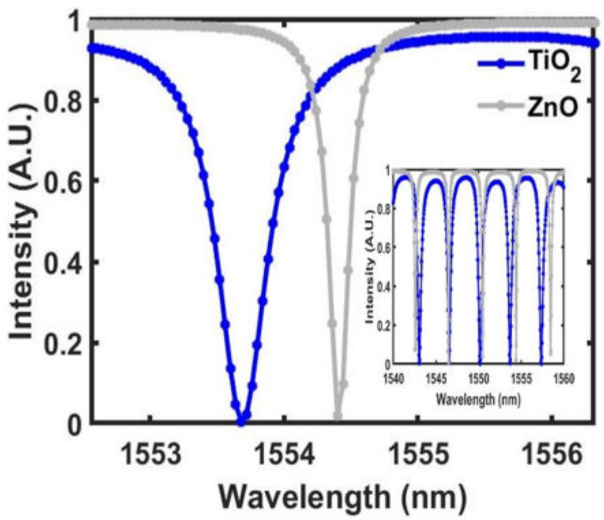

FIGURE 8. Transmission wavelength spectrum of AOR from 1552 nm to 1556 nm wavelength range for 60 μm ring radius of ZnO ($h = 500$ nm, $w = 1400$ nm, $d_g = 500$ nm) and TiO_2 ($h = 390$ nm, $w = 700$ nm, $d_g = 500$ nm) with a resonant wavelength of 1554.4 nm and 1553.68 nm respectively.

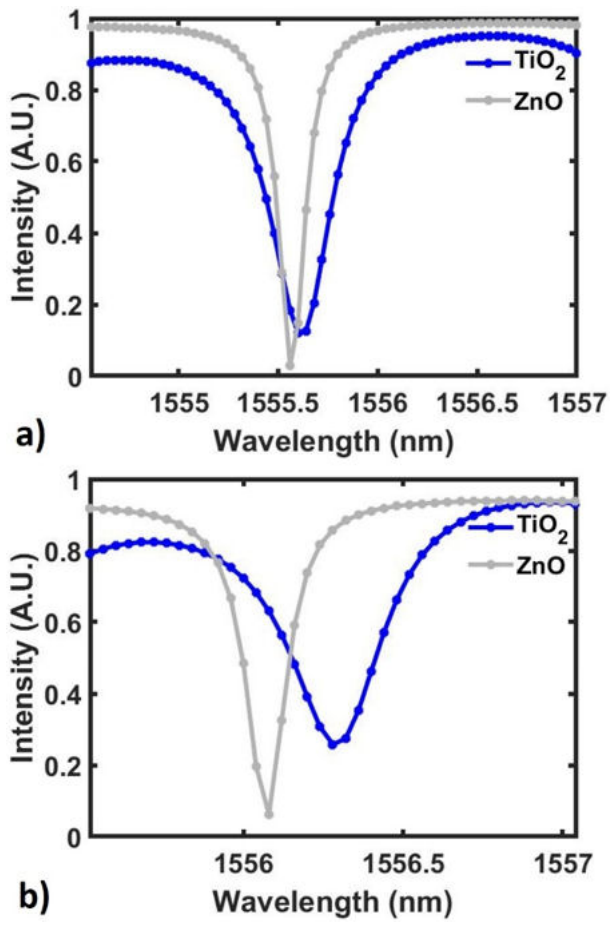

FIGURE 9. Transmission graph for the AOR from the telecommunication wavelength range: a) optical ring radius of 120 μm, b) optical ring radius of 180 μm.

As shown in Fig. 6, it is important to mention that the extinction ratio depends on the distance gap; then, it is necessary to consider the distance gap and the minimum bending losses to calculate the optimum performance of the AOR. At this point, the optimal configuration for a ring resonator with low losses, high excitation ratio, suitable $\mathrm{Q-factor}$, good finesse, and a narrow linewidth is the platform of ZnO material with a ring radius of 180 μm, d_g 500 nm using a 1400 nm width and 500 nm thin layer for cross-section with a cladding of air and substrate of SiO_2. It is important to recall that TiO_2 platform is also competitive and can be used for different applications. Table V compares prior studies in optoelectronic devices; as can be appreciated, the silicon-on-insulator platform is the standard material for subwavelength structures.

Several studies have successfully applied the ALD technique to deposit thin layers for fabricating optical ring resonators, focusing on slot waveguides achieving subwavelength structures [47–49]. It is important to highlight that this manuscript focuses on core materials synthesized through ALD, specifically ZnO and $\mathrm{TiO_2}$, for subwavelength optical channel structures in telecommunications applications. The proposed platform achieves low propagation losses and a high-quality factor, eliminating the need for a second ALD deposition step, as the previous works mentioned before.

4. Conclusion

Ring resonators based on optical channel waveguides using ALD materials (ZnO and $\mathrm{TiO_2}$) were analyzed by numerical simulation. The studies herein were conducted to propose a suitable platform: cross-section channel waveguide analysis, effective field distribution, and filtering analysis. By extrapolating methods, the following refractive index values at 1550 nm were computed: 2.36372 ($\mathrm{TiO_2}$) and 1.88581 (ZnO). The cross-section channel waveguide area to propagate fundamental modes with a cladding (Air) and substrate ($\mathrm{SiO_2}$) for a core were: ZnO (width: 1400 nm and thickness: 500 nm) and $\mathrm{TiO_2}$ (width: 700 nm and thickness: 390 nm). Here, the TE_0 n_{eff} values were obtained: 1.5946 (ZnO) and 1.7732 ($\mathrm{TiO_2}$). The maximum evanescent wave distance for each channel waveguide at 0.01% was: 855 nm (ZnO) and 716 nm ($\mathrm{TiO_2}$). Passing to the filtering study for the notch filter application, with their resolution analysis, $\mathrm{d_g}$ was 100 nm ranging from 200 nm to 600 nm, at the wavelength telecommunication range (C Band-1528 nm to 1566 nm) for a 60 $\mu\mathrm{m}$ ring radius, the optimal distance gap for each configuration was 500 nm. The following optical parameters were obtained: ZnO (λ_{res}: 1554.4 nm, FWHM: 0.2218 nm, Bending losses: -19.4699 dB/cm, and $\mathrm{Q-Factor}$: 7005) and $\mathrm{TiO_2}$ (λ_{res}: 1553.68 nm, FWHM: 0.4396 nm, Bending losses: -0.9708 dB/cm, and $\mathrm{Q-Factor}$: 3533). Being the quality factor a variable to improve, deciding for a new study focused on a 120 $\mu\mathrm{m}$ and 180 $\mu\mathrm{m}$ ring radius, which resulted in the best configuration platform of ZnO with a 180 $\mu\mathrm{m}$ ring radius. Here, the optical parameters were obtained

(λ_{res}: 1554.76 nm, FWHM: 0.1210 nm, Bending losses: -7.3069 dB/cm, and $\mathrm{Q-Factor}$: 12842). This platform is optimally designed for notch filter application in telecommunication. However, its characteristics may also be suitable for bio-sensing and micro-laser cavities. This proves that the ALD technique grows high refractive index materials, and considering the parameters of electron beam lithography manufacture can turn out to be a compact and efficient optical platform that can be integrated into chips and increase manufacturing quality. The results show that ZnO waveguide structures, with a ring radius as small as 60 $\mu\mathrm{m}$, can exceed the quality factor value proposed. In contrast, $\mathrm{TiO_2}$ structures required a ring radius up to 180 $\mu\mathrm{m}$ to surpass the quality factor threshold of 5000.

Appendix

The next boundary conditions equations were used to solve electric, magnetic, and intensity distribution fields to analyze the cross-section channel waveguide to calculate the following parameters: modal numbers, effective refractive index, confinement factor modal, and evanescent wave distribution. The boundary mode analysis condition displayed in Eq. (9) was used to solve using the wave equation:

$$\nabla \times (\nabla \times \mathbf{E}) - k_0^2 n^2 \mathbf{E} = 0, \tag{9}$$

where the electric field ($\mathbf{E}$), wave number of free space (k_0) and refractive index (n). The next sub-interfaces are the perfect electric and magnetic conductor as shown in the next equations:

$$n \times \mathbf{E} = 0, \tag{10}$$

$$n \times \mathbf{H} = 0, \tag{11}$$

where the magnetic field ($\mathbf{H}$). These boundary conditions focus on a particular case that sets the tangential component of the electric and magnetic field to zero.

Once we obtained information about our straight channel optical waveguides, the following interface was used to design the optical resonant filter, which considers the equations to solve unidirectional and bidirectional electromagnetic beam propagation. The subsequent mode analysis boundaries related to the wave equation, as shown in Eq. (12):

$$(\nabla - jk) \times ((\nabla - jk) \times \mathbf{E}) - k_0^2 (n^2) \mathbf{E} = 0, \tag{12}$$

In the wave equation, the beam envelope node is the central node, where the wave equations have an envelope function, where the current (j) and (k) are the wave number in the medium. The perfect electric conductor has been explained in the previous interface in Eq. (10). The Gaussian beam propagation port boundary is used where electromagnetic energy enters or exits the model, as shown in Eq. (13):

$$n \times \nabla \times \mathbf{E} - j\beta n \times \mathbf{E} \times n = 0, \tag{13}$$

where the propagation constant (β). The scattering boundary condition makes a boundary transparent for scattered wave, as explained in Eq. (14):

$$\begin{aligned} & n \times (\nabla \times \mathbf{E}) - (ik) n \times (\mathbf{E} \times n) \\ & = -n \left(\mathbf{E}_0 \times [(ik)n - ik] \right) e^{-ijk}, \end{aligned} \tag{14}$$

Finally, the field continuity assures that the tangential electric and magnetic field components are continuous on interior boundaries, assuming that $E_{T,1} = E_{T,2}, H_{T,1} = H_{T,2}$, where $E_{T,1}$, $H_{T,1}$, $E_{T,2}$, and $H_{T,2}$ are the electric and magnetic components fields from structure number 1 and 2, respectively [50].

Acknowledgments

J.D Castro-Toscano is grateful to CONAHCyT for the scholarship number 776661 (CVU: 832744). The authors would like to acknowledge the financial support given by DGAPA-UNAM through the PAPIIT research projects: IN108821, IN119023. In addition, financial support was provided by CONAHCyT through the FORDECyT 272894, SENER-CONACyT 117373. Also, to CONACyT A1-S-21084, A1-S-26789, A1-S-21323. Finally, the authors would like to acknowledge D. Domínguez, F. Ruiz, J. Mendoza, J. A. Díaz, I. Gradilla, E. Murillo, and E. Aparicio for technical assistance. M.I. Pérez Montfort corrected the English version of the manuscript. J.D Castro- Toscano appreciated the motivation by Lydia Toscano-Palomar.

AOR spectral response was obtained using COMSOL®, a software that uses a finite element method (FEM), *i.e.*, a numerical method to approximate solutions of differential equations for complex geometries. FEM employs a weak formulation of the differential equations to be represented as their integral form. COMSOL® manages different models to solve phenomenological physics.

1. M. H. Sani, S. Khosroabadi, and A. Shokouhmand, A novel design for 2-bit optical analog to digital (A/D) converter based on nonlinear ring resonators in the photonic crystal structure, *Optics Communications*, **458** (2020) 124760. `https://doi.org/10.1016/j.optcom.2019.124760`.
2. J. Meng, M. Miscuglio, J. K. George, A. Babakhani, and V. J. Sorger, Electronic bottleneck suppression in next-generation networks with integrated photonic digital-to-analog converters, *Advanced Photonics Research* **2** (2021) 2000033. `https://doi.org/10.1002/adpr.202000033`.
3. M. Hamidah and R. W. Purnamaningsih, An S-bend based optical directional coupler using GaN semiconductor, *2019 IEEE*

International Conference on Innovative Research and Development (ICIRD), (2019) 1-4. https://doi.org/10.1109/ICIRD47319.2019.9074743.

4. R. W. Purnamaningsih, N. R. Poespawati, T. Abuzairi, and E. Dogheche, An optical power divider based on mode coupling using GaN/Al_2O_3 for underwater communication, *Photonics*, **6** (2019) 063, https://doi.org/10.3390/photonics6020063.
5. V. Zamora, P. Lützow, M. Weiland, and D. Pergande, Investigation of cascaded SiN microring resonators at 1.3 μm and 1.5 μm, *Optics Express*, **21** (2013) 27550, https://doi.org/10.1364/OE.21.027550.
6. F. M. Prat *et al.*, Self-referenced sensor, *Google Patents*, (2022).
7. V. Melissinaki, O. Tsilipakos, M. Kafesaki, M. Farsari, and S. Pissadakis, Micro-ring resonator devices prototyped on optical fiber tapers by multi-photon lithography, *IEEE Journal of Selected Topics in Quantum Electronics* **27** (2021) 1, https://doi.org/10.1109/JSTQE.2021.3062716.
8. W. Bogaerts *et al.*, Silicon microring resonators, *Laser and Photonics Reviews* **6** (2012) 47, https://doi.org/10.1002/lpor.201100017.
9. P. Girault *et al.*, Integrated polymer micro-ring resonators for optical sensing applications, *Journal of Applied Physics*, **117** (2015) 4914308, https://doi.org/10.1063/1.4914308.
10. L. Chang, M. de Goede, M. Dijkstra, C. I. van Emmerik, and S. M. García-Blanco, Modular microring laser cavity sensor, *Optics Express*, 29 (2021) 1371, https://doi.org/10.1364/OE.411811.
11. C. Vieu *et al*., Electron beam lithography: resolution limits and applications, *Applied Surface Science*, **164** (2000) 111-117. https://doi.org/10.1016/S0169-4332(00)00352-4.
12. J. A. Jurado-González *et al*., TiO_{2-x} films as a prospective material for slab waveguides prepared by atomic layer deposition, *Optics & Laser Technology*, **158** (2023) 108880. https://doi.org/10.1016/j.optlastec.2022.108880.
13. H. A. Borbón-Nuñez, D. Dominguez, F. Muñoz-Muñoz, J. Lopez, J. Romo-Herrera, G. Soto, and H. Tiznado, Fabrication of hollow TiO_2 nanotubes through atomic layer deposition and MWCNT templates, *Powder Technology* **308** (2017) 249-257. https://doi.org/10.1016/j.powtec.2016.12.001.
14. E. G. Lizárraga-Medina *et al*., Optical waveguides fabricated in atomic layer deposited Al_2O_3 by ultrafast laser ablation, *Results in Optics* **5** (2021) 100060. https://doi.org/10.1016/j.rio.2021.100060.
15. V. Donzella, A. Sherwali, J. Flueckiger, S. M. Grist, S. T. Fard, and L. Chrostowski, Design and fabrication of SOI microring resonators based on sub-wavelength grating waveguides, *Optics Express* **23** (2015) 4791. https://doi.org/10.1364/oe.23.004791.
16. T. Barwicz *et al*., Microring-resonator-based add-drop filters in SiN: Fabrication and analysis. *Optics Express*, **12** (2004) 1437-1442. https://doi.org/10.1364/OPEX.12.001437
17. G. M. Hasan *et al.*, Ring resonator gap determination design rule and parameter extraction method for sub-GHz resolution whole C-band Si_3N_4 integrated spectrometer. *Photonics*, **9** (2022) 51. https://doi.org/10.3390/photonics9090651
18. M. Fu *et al*., High-Q titanium dioxide micro-ring resonators for integrated nonlinear photonics. *Optics Express* **28** (2020) 39084. https://doi.org/10.1364/oe.404821
19. Z. Chen, *et al*., Efficient and compact sol-gel TiO_2 thermo-optic microring resonator modulator. *Optical Materials Express* **12** (2022) 4061. https://doi.org/10.1364/ome.472722
20. X. Zhang, Z. Li, Y. Sun, and K. Tong, Simulation of ZnO-coated SOI microring resonant shift response to ethanol and ammonia. *Optik*, **125** (2014) 2752, https://doi.org/10.1016/j.ijleo.2013.11.037
21. C. Jiang, C. Tang, and J. Song, The smallest resonator arrays in atmosphere by chip-size-grown nanowires with tunable Q-factor and frequency for subnanometer thickness detection. *Nano Letters*, **15** (2015) 1128, https://doi.org/10.1021/nl504135x
22. D. L. Caballero-Espitia *et al.*, Study of Al_2O_3 thin films by ALD using H_2O and O_3 as oxygen source for waveguide applications. *Optical Materials* **109** (2020) 110370. https://doi.org/10.1016/j.optmat.2020.110370
23. B. López *et al*., Third-order nonlinear optical properties of a multi-layer Al_2O_3/ZnO for nonlinear optical waveguides. *Optics Express* **27** (2019) 17359-17368. https://doi.org/10.1364/OE.27.017359
24. D. Rabus, *Integrated ring resonators: The compendium*. (Springer 2007). https://doi.org/10.1007/978-3-540-68788-7
25. P. O. Oviroh, R. Akbarzadeh, D. Pan, R. A. M. Coetzee, and T. C. Jen, New development of atomic layer deposition: Processes, methods and applications. *Science and Technology of Advanced Materials*, **20** (2019) 465-496. https://doi.org/10.1080/14686996.2019.1599694:
26. B. Sanchez, *Diseño, fabricación y caracterización de guías de onda ópticas de óxido de zinc*. [Master's thesis]. Centro de Investigación Científica y de Educación Superior (2023).
27. T. Tran, V. A. Pham, P. Le, T. Nguyen, and V. Tran, Synthesis of amorphous silica and sulfonic acid functionalized silica used as reinforced phase for polymer electrolyte membrane. *Advanced Natural Science: Nanosci. Nanotechnol.*, **4** (2013) 045007, https://doi.org/10.1088/2043-6262/4/4/045007
28. T. Rajakaruna, C. Udawatte, R. Chandrajith, and R. Rajapakse, Nonhazardous process for extracting pure titanium dioxide nanorods from geogenic ilmenite. *ACS Omega* (2020). https://doi.org/10.1021/acsomega.0c01756
29. G. Valverde-Aguilar, and J. Zepeda, Photoluminescence and photoconductivity studies on amorphous and crystalline ZnO thin films obtained by sol-gel method. *Applied Physics A*, **118** (2014) 1305, https://doi.org/10.1007/s00339-014-8836-y

30. A. Kaushalram, G. Hegde, and S. Talabattula, Mode hybridization analysis in thin film lithium niobate strip multimode waveguides. *Scientific Reports* **10** (2020). https://doi.org/10.1038/s41598-020-73936-x

31. S. Jahani, Controlling evanescent waves using silicon photonic all-dielectric metamaterials for dense integration. *Nature Communications* **9** (2018) 8, https://doi.org/10.1038/s41467-018-04276-8

32. X. Wu, and L. Tong, Optical microfibers and nanofibers. *Nanophotonics* **2** (2013) 407-428. https://doi.org/10.1515/nanoph-2013-0033

33. R. Castillo-Perez *et al*., Comparative modal analysis in micro-nano-optical fiber tapers using spectral parameter power series method and exact modes method. *Journal of Computational Electronics* **22** (2023) 690, https://doi.org/10.1007/s10825-023-02006-y

34. X. Cheng, J. Hong, A. M. Spring, and S. Yokoyama, Fabrication of a high-Q factor ring resonator using LSCVD deposited Si_3N_4 film. *Optical Materials Express*, **7** (2017) 2182, https://doi.org/10.1364/OME.7.002182

35. P. Cheben, D.-X. Xu, S. Janz, and A. Densmore, Subwavelength waveguide grating for mode conversion and light coupling in integrated optics. *Optics Express*, **14** (2006) 4695-4702. https://doi.org/10.1364/OE.14.004695

36. L. Sun, Y. Zhang, Y. He, H. Wang, and Y. Su, Subwavelength structured silicon waveguides and photonic devices. *Nanophotonics*, **9** (2020) 1321, https://doi.org/10.1515/nanoph-2020-0070

37. L. R. Chen, J. Wang, B. Naghdi, and I. Glesk, Subwavelength grating waveguide devices for telecommunications applications. *IEEE Journal of Selected Topics in Quantum Electronics*, **25** (2019) 1, https://doi.org/10.1109/JSTQE.2018.2879015

38. J. Haas, P. Artmann, and B. Mizaikoff, Mid-infrared GaAs/AlGaAs micro-ring resonators characterized via thermal tuning. *RSC Advances*, **9** (2019) 8594, https://doi.org/10.1039/C8RA10395J

39. P. P. Absil *et al*., Wavelength conversion in GaAs micro-ring resonators. *Optics Letters*, **25** (2000) 554, https://doi.org/10.1364/OL.25.000554

40. R. Armand *et al*., Mid-infrared integrated silicon-germanium ring resonator with high Q-factor. *APL Photonics*, **8** (2023) 071301. https://doi.org/10.1063/5.0149324

41. R. Morgan, C. Heidelberger, D. Kharas, K. Cahoy, and C. Sorace-Agaskar, Low-loss germanium-on-silicon waveguides and ring resonators for the mid-wave infrared. In *Conference on Lasers and Electro-Optics, Technical Digest Series* (Optica Publishing Group), paper SW5O.1. (2022).

42. M. Furuhashi Development of microfabricated TiO_2 channel waveguides. *AIP Advances* **1** (2011), https://doi.org/10.1063/1.3615716

43. C. Evans, C. Liu, and J. Suntivich, Low-loss titanium dioxide waveguides and resonators using a dielectric lift-off fabrication process. *Optics Express*, **23** (2015) 11160, https://doi.org/10.1364/OE.23.011160

44. M. Fu *et al.*, High-Q titanium dioxide micro-ring resonators for integrated nonlinear photonics. *Optics Express*, **28** (2020) 39084, https://doi.org/10.1364/oe.404821

45. Y. Shen *et al.*, Femtosecond laser writing of waveguides in zinc oxide crystals: Fabrication and mode modulation. *Optics Express*, **30** (2022) 27694, https://doi.org/10.1364/OE.30.027694

46. P. Struk *et al*., Planar optical waveguides based on thin ZnO layers. *Acta Physica Polonica Series A*, **116** (2009) 68, https://doi.org/10.12693/APhysPolA.116.414

47. A. Autere *et al*., High-quality slot waveguide ring resonator based on atomic layer deposition. *Proceedings of SPIE - The International Society for Optical Engineering*, **9367** (2015), https://doi.org/10.1117/12.2076903

48. A. Autere *et al*., Slot waveguide ring resonators coated by an atomic layer deposited organic/inorganic nanolaminate. *Optics Express*, **23** (2015) 26940, https://doi.org/10.1364/OE.23.026940

49. M. Fu *et al*., High-Q titanium dioxide micro-ring resonators for integrated nonlinear photonics. *Optics Express* **28** (2020) 39084, https://doi.org/10.1364/oe.404821

50. COMSOL. (2018). *Wave Optics Module User's Guide* (COMSOL 5.4). Retrieved from https://doc.comsol.com/5.4/doc/com.comsol.help.woptics/WaveOpticsModuleUsersGuide.pdf